Title

Solar anti-icing surface with enhanced condensate self-removing at extreme environmental conditions

Journal

Proceedings of the National Academy of Sciences of the United States of America, 118(18)

ISSN

0027-8424

Authors

Zhang, Hongqiang
Zhao, Guanlei
Wu, Shuwang
et al.

Publication Date

2021-05-04

DOI

10.1073/pnas.2100978118

Peer reviewed

Solar anti-icing surface with enhanced condensate self-removing at extreme environmental conditions

Hongqiang Zhang[a,1], Guanlei Zhao[b,c,1], Shuwang Wu[d], Yousif Alsaid[d], Wenzheng Zhao[c], Xiao Yan[e], Lei Liu[c], Guisheng Zou[c], Jianyong Lv[b], Ximin He[d,2], Zhiyuan He[b,2], and Jianjun Wang[b]

[a]School of Mechanical Engineering and Automation, Beihang University, 100191 Beijing, China; [b]Institute of Chemistry, University of Chinese Academy of Sciences, 100190 Beijing, China; [c]Department of Mechanical Engineering, Tsinghua University, 100084 Beijing, China; [d]Department of Materials Science and Engineering, University of California, Los Angeles, CA 90095; and [e]Department of Mechanical Science and Engineering, University of Illinois at Urbana–Champaign, Urbana, IL 61801

Edited by David A. Weitz, Harvard University, Cambridge, MA, and approved March 21, 2021 (received for review January 17, 2021)

The inhibition of condensation freezing under extreme conditions (i.e., ultra-low temperature and high humidity) remains a daunting challenge in the field of anti-icing. As water vapor easily condensates or desublimates and melted water refreezes instantly, these cause significant performance decrease of most anti-icing surfaces at such extreme conditions. Herein, inspired by wheat leaves, an effective condensate self-removing solar anti-icing/frosting surface (CR-SAS) is fabricated using ultrafast pulsed laser deposition technology, which exhibits synergistic effects of enhanced condensate self-removal and efficient solar anti-icing. The superblack CR-SAS displays superior anti-reflection and photothermal conversion performance, benefiting from the light trapping effect in the micro/nano hierarchical structures and the thermoplasmonic effect of the iron oxide nanoparticles. Meanwhile, the CR-SAS displays superhydrophobicity to condensed water, which can be instantly shed off from the surface before freezing through self-propelled droplet jumping, thus leading to a continuously refreshed dry area available for sunlight absorption and photothermal conversion. Under one-sun illumination, the CR-SAS can be maintained ice free even under an ambient environment of −50 °C ultra-low temperature and extremely high humidity (ice supersaturation degree of ∼260). The excellent environmental versatility, mechanical durability, and material adaptability make CR-SAS a promising anti-icing candidate for broad practical applications even in harsh environments.

anti-icing | photothermal | condensate self-removal | ultrafast pulsed laser deposition | surface micro-/nano-structuring

Condensation freezing/frosting on solid surfaces causes severe economic and safety issues. Thus, highly efficient anti-icing/frosting approaches are vital in many engineering applications, ranging from air conditioners to power transmission systems (1–4). Tremendous efforts have been invested into designing active and passive anti-icing surfaces. Active anti-icing strategies including mechanical, chemical, and thermal methods often consume high amounts of energy and require specific facilities for deicing, which limit their practical applications (5, 6). Passive anti-icing surfaces involve strategies to delay and inhibit ice formation, such as hydrated surfaces, lubricant-infused surfaces, bioinspired anti-freezing surfaces, and superhydrophobic surfaces (SHSs) (3, 7–13). Although these passive icephobic materials offer numerous advantages to prevent ice accretion, each comes with its own limitations (14).

At extreme environmental conditions where condensation and desublimation are strongly promoted, an optimal passive anti-icing surface should immediately remove condensed water droplets and leave no water for freezing. To prepare such a kind of surface, lots of efforts have been made to study the abilities of SHSs for removing condensed water. However, regular SHSs are incapable of removing microscale condensed water droplets under humid conditions due to the wetting of surface micronanostructures, which leads to the formation of highly pinned Wenzel droplets and the loss of superhydrophobicity (15–17). Tremendous investigations have shown that SHSs with specially designed structures can retain superhydrophobicity to condensed water droplets, and coalesced droplets can be spontaneously removed from the surface via self-propelled jumping (18–20). The self-propelled jumping of condensed droplets is driven by the released surface energy during droplet coalescence after overcoming solid–liquid adhesion (21–25). However, these surfaces inevitably lose their water repellency at low temperatures (i.e., < -15 °C) because of freezing (9, 21, 26). Thus, it is highly desirable to design new anti-icing surfaces that can maintain capability for removing the condensed water at extreme environmental conditions, which is highly important for anti-icing applications in many scenarios (i.e., aircrafts flying through clouds, wind turbines operating in winter, and power transmission facilities working in extremely cold and humid regions) (27).

Recently, intensive research efforts have been dedicated to solar anti-icing/frosting surfaces (SASs), which can absorb sunlight efficiently and convert solar energy to heat, thereby delaying or preventing ice formation (28–30). Because of its effective utilization of clean and renewable solar energy, SASs are environmentally

Significance

Among various anti-icing conditions, cold and humid environments are the most difficult to tackle. Although photothermal materials have been used to increase surface temperature for delaying freezing, severe condensation under cold and humid environments causes increased reflection, resulting in lower temperature rise and eventually condensate freezing. Ideal passive anti-icing surfaces should remove condensed water immediately, leaving no water for freezing. Herein, a condensate self-removing solar anti-icing/frosting surface is developed. With optimum hierarchical micro/nanostructures, it has excellent photothermal capability to elevate surface temperature and simultaneously can shed off condensed water effectively via coalescence-induced droplet jumping, providing continuously refreshed dry surface for sunlight absorption to maintain the elevated temperature under challenging environmental conditions, where condensation and fogging would otherwise be strongly promoted.

Author contributions: H.Z., G. Zhao, X.H., Z.H., and J.W. designed research; H.Z. performed research; W.Z., X.Y., L.L., and G. Zou contributed new reagents/analytic tools; H.Z., G. Zhao, S.W., Y.A., J.L., X.H., Z.H., and J.W. analyzed data; and H.Z., G. Zhao, S.W., Y.A., J.L., X.H., Z.H., and J.W. wrote the paper.

The authors declare no competing interest.

This article is a PNAS Direct Submission.

[1]H.Z. and G. Zhao contributed equally to this work.

[2]To whom correspondence may be addressed. Email: ximinhe@ucla.edu or hezy@iccas.ac.cn.

This article contains supporting information online at https://www.pnas.org/lookup/suppl/doi:10.1073/pnas.2100978118/-/DCSupplemental.

Published April 26, 2021.

friendly and energy efficient. Notably, a number of photothermal conversion materials including carbon materials, conjugated polymers, two-dimensional nanostructural materials, and metallic particles have also been applied as SASs (28, 31–34). Although remarkable improvements have been made, some challenges have yet to be tackled. For instance, most of the reported SASs cannot remove the condensed water effectively, particularly in cold and humid conditions (35, 36). The accumulation of the condensed water would significantly enhance reflectance leading to reduced photothermal efficiency (37) and decreased temperature. As a result, frost formation through the freezing of condensed water (condensation frosting) will prevent sunlight from reaching the SAS, resulting in the complete loss of its photothermal capability: as light harvesting becomes less efficient, the temperature of the SAS decreases, resulting in a vicious compounding cycle of condensation freezing. Moreover, the contaminants on the SAS can also inhibit sunlight absorption (38). Therefore, it is desirable to develop highly photothermal–efficient SASs with the abilities of removing condensed water to maintain high temperature and self-cleaning for avoiding blockage of sunlight by contaminants.

Herein, we present a proof-of-concept SAS with synergistically binary effects of enhanced condensate self-removing and efficient solar anti-icing. We fabricated hierarchically structured materials using ultrafast pulsed laser deposition (PLD) technology. Low-effective refractive index and multilayered iron oxide structures endow the material with broadband ultralow reflectance and high solar-to-heat conversation efficiency. The hierarchically structured SHS demonstrated the capability of removing condensates before freezing via self-propelled droplet jumping induced by droplet coalescence and evaporation flux under heating. The sustained shedding of condensed water droplets resulted in a continuously refreshed, dry and clean area available for efficient sunlight absorption and photothermal conversion; the temperature of the condensate self-removing solar anti-icing/frosting surface (CR-SAS) could be constantly maintained above the freezing temperature, which in turn ensured high-performance water repellency. With such synergistic mutual-benefitting effects of condensate self-removal and photothermal heating, under one-sun illumination, the CR-SAS remained ice-free even at an ambient temperature (T_a) of −50 °C and ultra-high humidity with a supersaturation degree (SSD) of ∼260, demonstrating superior anti-icing performances under extremely harsh operating conditions.

Results

Fabrication of CR-SASs. Some aquatic plant leaf surfaces typically exhibit hydrophobic and self-cleaning properties for removing water droplets and dust, thus leading to more efficient sunlight absorption in a wet environment. As schematically illustrated in Fig. 1*A*, wheat leaves display self-propelled jumping of microdroplets and self-removal of contaminants through droplet mutual coalescence, leaving more clean and dry-leaf surface area available for photosynthesis (39). Inspired by wheat leaves, we have fabricated hierarchically structured SASs with synergistic binary effects of enhanced condensate self-removing and efficient solar anti-icing, herein designated as CR-SASs. The CR-SASs were constructed by facilely depositing a layer of iron oxide nanoparticles on copper substrates using a PLD system (*Materials and Methods*). Briefly, high-intensity laser pulses were irradiated onto an iron target inside a vacuum chamber filled with a small amount of argon (Ar) gas to induce material ablation, generating a plasma plume primarily consisting of atoms, nanoparticles, and other energetic particulates (40). The plasma plume, containing iron nanoparticles, was sputtered away from the iron target and collided with Ar molecules inside the vacuum chamber. The inhomogeneous collision resulted in varying deceleration rates of nanoparticles, forming a porous hierarchically structured layer upon deposition on the substrate. In addition, at higher Ar pressures, the nanoparticles exhibit a higher collision probability with Ar molecules, resulting in nanoparticles with lower velocity that tend to form structures with higher porosity. Therefore, by adjusting the Ar pressure within the vacuum chamber, the porosity and the morphology of the deposited layer can be easily controlled (41, 42). After PLD, the as-prepared hierarchical structured surface was oxidized into a superblack layer consisting of iron oxide nanoparticles under atmospheric condition (43). Lastly, the hierarchically structured superblack surfaces were modified with perfluorodecyltrimethoxysilane to obtain superhydrophobicity.

The as-prepared CR-SASs displayed similar behaviors with wheat leaf (Fig. 1*A*) (i.e., the superblack surface was hierarchically designed for achieving both functions of enhanced condensate self-removal and sunlight absorption). The microscale structures provided more light traps and longer light trajectories to induce multiple internal reflections, thus leading to superior anti-reflection performance and high solar-to-heat efficiency. Moreover, to mimic the condensate self-removing capability of wheat leaves, special nanoscale structures were fabricated, and the surface superhydrophobicity can be maintained under a condensing condition. The presence of surface nanostructural features inhibit the wetting of condensed microdroplets while reducing solid–liquid adhesion, which enables the removal of condensates from the surface via droplet mutual coalescence (44, 45). Meanwhile, the jumping is also boosted by the efficient photothermally induced evaporation of the condensed water, in which the high vapor flux, confined by the rationally designed hierarchical structure, uniquely promotes the spontaneous droplet levitation (46). Overall, the heat-induced vaporization inside the microstructure and the ultralow adhesion at the solid/liquid interface promote spontaneous droplet jumping synergistically. This ensures the melted and/or condensed water can be continuously removed from the surface, leaving the surface always clean, dry, and uncovered, which is critical for efficient solar absorption. Fig. 1 *B* and *C* and *SI Appendix*, Fig. S1 show the top-view and side-view images of CR-SASs with applied Ar pressures of 10 Pa (H10), 20 Pa (H20), and 30 Pa (H30). H10 displays a compact, cauliflower-like morphology. As the Ar pressure gradually increased, the hierarchical structure became looser and more porous, leading to the formation of sponge-like structures on the H30 surface. In addition, the layer thickness increased with higher Ar pressure, and the layer thicknesses of H10, H20, and H30 are ∼1.0 μm, 2.0 μm, and 2.8 μm, respectively. At last, all the hierarchically structured surfaces displayed contact angles of more than 150° and a tilting angle of around 2°, as shown in the insets of Fig. 1*B* and *SI Appendix*, Fig. S2.

The surface composition of hierarchically structured CR-SASs is shown in *SI Appendix*, Fig. S3. The depth profiling of CR-SASs was characterized by X-ray photoelectron spectroscopy (XPS) combined with ion sputtering, and the Fe 2p XPS spectra of H30 at different depths under the surface was obtained (*SI Appendix*, Fig. S4). As schematically illustrated in Fig. 1*C*, the top layer of the H30 surface primarily consists of Fe_2O_3. The oxygen content decreases with increasing depth, indicating that the formation of iron oxide nanoparticle layer was indeed through oxidation of deposited iron nanoparticles.

Condensate Self-Removal. Under cold and humid conditions, the accretion of condensates on ordinary SASs can absorb and reflect incident sunlight, thereby significantly reducing photothermal conversion efficiency of SASs. Hence, it is highly desirable to continuously remove condensed water off SASs to maintain stable and efficient solar energy harvesting. Remarkably, owing to reduced contact area and ultra-low water/solid adhesion enabled by specially constructed nanoscale structures, the prepared CR-SASs displayed condensate self-removal driven by the released surface energy via

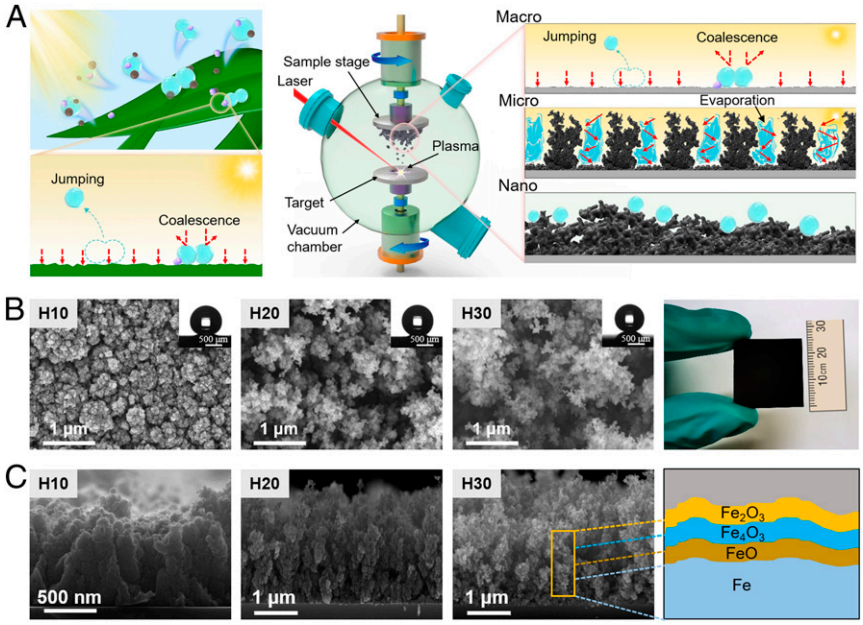

Fig. 1. Fabrication and characterization of CR-SASs. (*A*) Schematic illustration of the CR-SAS fabrication process through PLD. The as-prepared hierarchically structured CR-SASs display condensate self-removing capability, induced by droplet coalescence and vaporization under heating, leading to continuously refreshed, dry, and clean area available for sunlight absorption, similar to wheat leaves. CR-SASs also exhibit high sunlight absorption efficiency due to the light trapping effect from surface microstructures. (*B*) Top-view microscopic and macroscopic images of superblack CR-SASs with applied Ar pressure of 10 Pa (H10), 20 Pa (H20), and 30 Pa (H30). (*C*) Side-view images of CR-SASs and their surface composition.

mutual droplet coalescence, as illustrated in Fig. 2 *A* and *B* (Movie S1 and *Materials and Methods*).

To further elucidate the self-removing capability of condensed water droplets, we studied the condensation process on different CR-SASs. As schematically illustrated in *SI Appendix*, Fig. S5, the condensation processes on CR-SASs within 10 min were recorded by an optical system coupled with a front-view and side-view high-speed camera (Movie S2). During the condensation experiment, samples were placed onto a cryostage with a temperature of 1.0 ± 0.5 °C to facilitate water condensing while preventing freezing. The ambient temperature (T_a) and relative humidity were 24.0 ± 1.0 °C and 40 ± 5%, respectively, corresponding to an SSD of 1.82. Then, the water removal rate (R_{wr}) and the fraction of dry area (f_{dry}) on CR-SASs were quantitatively

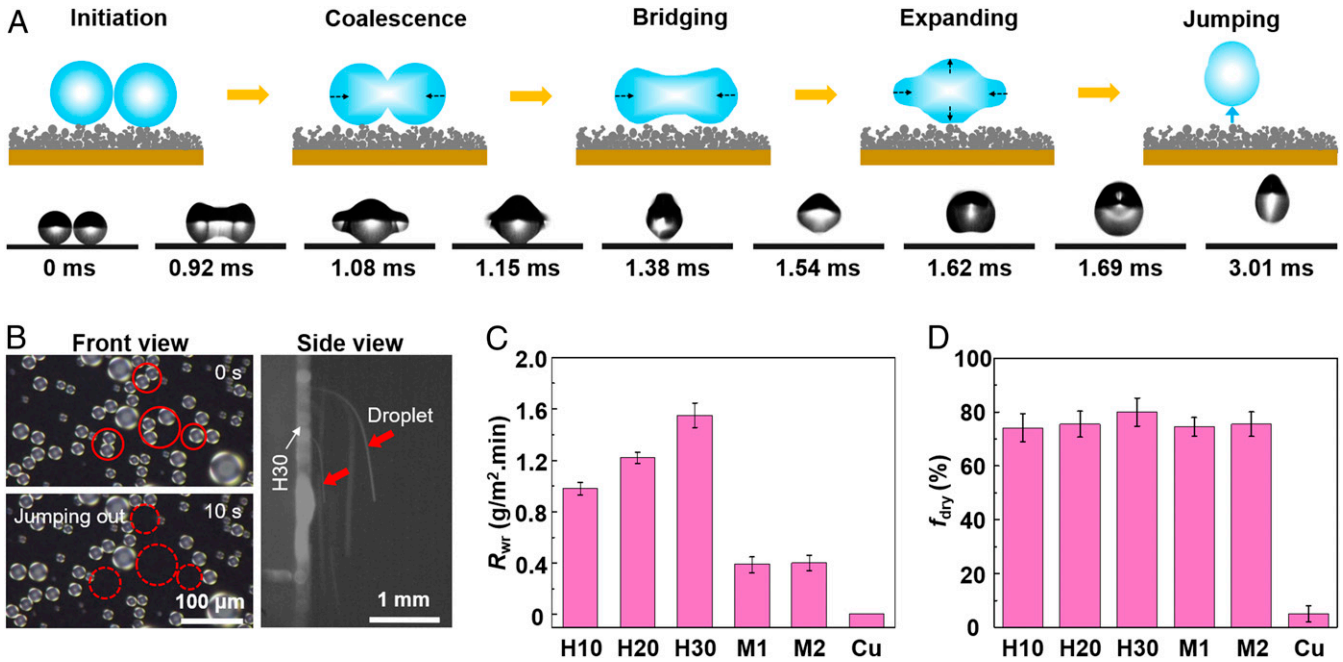

Fig. 2. Condensate self-removal of CR-SASs. (*A*) Schematic (top images) and experimental (bottom images) illustrations of the coalescence-induced droplet jumping process. (*B*) Condensed droplets can be continuously removed from CR-SASs through coalesced droplet jumping. (*C*) R_{wr} during 10 min condensation experiments for the prepared samples. (*D*) f_{dry} after prolonged condensation experiment for the prepared samples.

measured and analyzed using a previously developed algorithm (*Materials and Methods*) (47). In addition, to further demonstrate the effectiveness of the CR-SASs in remaining dry under condensing conditions, we conducted condensation experiments on bare copper (Cu) and microstructured (M1 and M2) surfaces with varying structural heights for comparison (*SI Appendix*, Fig. S6), and the results are detailed in Fig. 2 *C* and *D* and *SI Appendix*, Fig. S7.

As clearly seen in Fig. 2*C*, the highest R_{wr} of 1.6 g/m^2 min was observed on H30, as its loose surface nanostructures were optimal for condensate self-removal among the prepared samples (44, 45). Intuitively, the f_{dry} of a surface under condensing condition should be strongly dependent on the R_{wr}. As a result, the f_{dry} on all the CR-SASs (>70%) were significantly higher than the Cu surface (~5%), which did not display any coalesced droplet jumping (Fig. 2*D*). With the highest R_{wr}, H30 also exhibited the highest f_{dry} of around 80%, which indicates that the surface of H30 can remain mostly dry under a condensing environment. M1 and M2 were fabricated with ultrafast laser processing, hence nanostructures still formed on the surfaces, enabling some condensate self-removing capability (48). However, since the nanostructures were not properly tuned to promote droplet jumping, the water–self-removing capability was notably weaker than CR-SASs. At last, self-cleaning capability of CR-SASs is demonstrated in Movie S3, in which dust particles can be removed from the surface through self-propelled coalesced droplet jumping (49).

Photothermal Performance. In addition to condensate self-removal, the hierarchical structures consisting of iron oxide nanoparticles also endowed CR-SASs with superior anti-reflection and photothermal conversion abilities, due to the combined results of the light trapping effect from the micro/nano hierarchical structures and the thermoplasmonic effect of the iron oxide nanoparticles. Fig. 3*A* shows the reflection spectra measurements (295 to 2,500 nm) of H10, H20, H30, M1, M2, and Cu. Generally, CR-SASs, in particular the surfaces of H20 and H30, exhibited outstanding anti-reflection performance (i.e., the average reflectivity was <5.3% in the ultraviolet-visible region and <8.8% in the near infrared region). In strong contrast, the average reflectivity of Cu, M1, and M2 surfaces at the visible to infrared region were 94.1%, 77.7%, and 57.4%, respectively. Consequently, CR-SASs exhibited higher equilibrium temperatures under one-sun illumination (1 kW·m^{-2}) than other samples, which was consistent with the reflectance spectra results (Fig. 3*B*). The temperatures of the samples were recorded at an ambient temperature of 23.0 ± 1.0 °C with a relative humidity of 45 ± 5% (*Materials and Methods*). The equilibrium temperatures on the H10, H20, and H30 surfaces were 72.0 °C, 75.5 °C, and 78.9 °C, respectively (*SI Appendix*, Fig. S8).

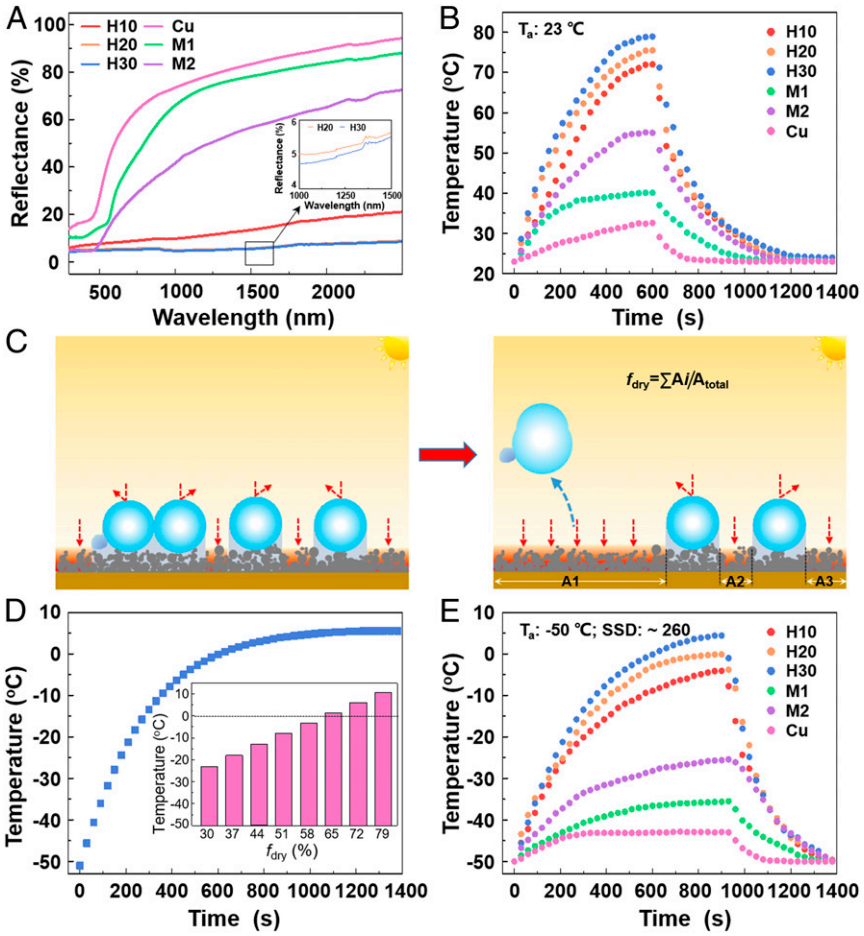

Fig. 3. Photothermal performance of CR-SASs. (*A*) Reflectance spectra of CR-SASs, M1, M2, and Cu. (*B*) Photothermal performance for each surface under one-sun illumination; the ambient temperature and the relative humidity are 23.0 ± 1.0 °C and 45 ± 5%, respectively. (*C*) Schematic illustration showing the influence of f_{dry} on photothermal capability of a surface under a condensing environment, in which the continuous removal of condensates is highly beneficial. (*D*) Simulated results for the temperature rise of surfaces with high f_{dry} (72%) in the low-temperature and high-humidity environment. The inset graph shows the simulated temperature rise of surfaces with different f_{dry} in the low-temperature and high-humidity condition. (*E*) Experimental results showing the photothermal performance of the samples in the low-temperature and high-humidity condition.

In comparison, the equilibrium temperatures of M1, M2, and Cu were only 40.1 °C, 55.0 °C, and 32.6 °C, respectively. The equilibrium temperatures of the samples under different solar illumination angles and solar intensities are also provided in *SI Appendix*, Fig. S9.

Besides the high anti-reflection property, an efficient CR-SAS should also inhibit the accumulation of condensates and contaminants for practical application. Note that the high light absorption efficiency could not be sustained under cold and humid environment because the presence of condensed water reflects most of the sunlight, leading to a massive drop in photothermal efficiency, as illustrated in *SI Appendix*, Fig. S10. The continuous and efficient water–self-removing capability of CR-SASs reduced the surface coverage of condensates over time, thus leading to a stable and large dry surface area on CR-SASs even under cold and humid environments. Consequently, incident light could be fully absorbed by their dry surfaces and efficiently converted to heat, owing to their superior anti-reflection and photothermal properties, as schematically illustrated in Fig. 3*C*. To elaborate, we employed a heat-transfer model based on the ANSYS FLUENT software to study the influence of f_{dry} on the photothermal capability of a surface with similar properties as H30 under one-sun illumination at −50 °C (*Materials and Methods* and *SI Appendix*, Fig. S11). The simulation condition closely imitated the experimental setup (i.e., samples were placed onto a thermally insulating plank [3 mm thick] in a closed quartz chamber at −50 °C). Fig. 3*D* shows that the simulated equilibrium temperatures on a photothermal surface with $f_{dry} = 72\%$ reached 5.5 °C within 1,400 s under one-sun illumination with an ambient temperature of −50 °C. The equilibrium temperature was over 0 °C as f_{dry} exceeded 65%, which indicates that a certain f_{dry} is indeed required for CR-SASs to remain unfrozen under a specific environmental condition (−50 °C and solar illumination of one sun).

Furthermore, the in situ photothermal processes on various surfaces under the low-temperature and high-humidity condition were investigated under one-sun illumination. It should be noted that this low-temperature and high-humidity condition was characterized by its extremely high SSD reaching ∼260, as illustrated in *SI Appendix*, Fig. S12 (*Materials and Methods*). From Fig. 3*E*, it is observed that only the equilibrium temperature of H30 exceeded 0 °C, attributed to its superior condensate self-removing capability (f_{dry} = 80%) and high photothermal conversion capability. It takes a large amount of heat to evaporate the condensed droplets under a condensing condition. Thus, the rates of temperature risen for the surfaces under a condensing condition are considerably slower than that under a dry condition. For instance, it took about 500 s to reach steady state on H30 surface under a dry condition, but more than 900 s were needed under a condensing condition. The equilibrium temperatures on H10, H20, M1, M2. and Cu surfaces were −4.1 °C, −0.1 °C, −35.5 °C, −25.4 °C, and −43 °C, respectively. Consequently, the M1, M2, and Cu surfaces were rapidly covered by a layer of condensates and ice/frost under such extreme experimental conditions.

Durability and Versatility of the CR-SASs. Industrial applications often require icephobic surfaces to be durable and versatile in harsh operating environments. We studied the photothermal and anti-icing performances of H30 surface under the low-temperature and high-humidity condition for an extended period of time and observed that no frost appeared under one-sun illumination, as shown in Fig. 4*A*. In strong contrast, ice/frost formation occurred on the Cu surface immediately, and the surface was entirely covered by a thick layer of frost after 10 min. To further elucidate the reason for effective solar anti-icing/frosting in H30, an infrared camera coupled with a magnifying lens was employed to investigate the dynamic water condensation, removal, and freezing process on the surface (*Materials and Methods*). As shown in Fig. 4*B*, unlike the Cu surface, the surface temperature of H30 remained above 0 °C due to continuous jumping of coalesced droplets under one-sun illumination. This efficient water removal via droplet jumping reduced the number and size of condensed droplets, which led to higher sunlight absorption on the dry surface. Thus, the reason for effective solar anti-icing/frost of H30 can be attributed to the dual effects of condensates' self-removal and efficient sunlight absorption.

The equilibrium temperatures on H30 surfaces under different humidities and solar illumination intensities were investigated (*Materials and Methods*). As the humidity at the chamber inlet was increased, the photothermal capacity of H30 remained relatively constant, as shown in Fig. 4*C*; this indicates that the higher condensation arising from higher humidity can be effectively counteracted by the self-propelled droplet jumping. We deduce that a higher abundance of coalescence removal events leads to similar f_{dry} on the H30 surface, despite differences in environmental humidity. Meanwhile, solar illumination intensity exerts more influence on temperature rise for H30, in which a decrease in solar illumination intensity led to notably lower surface temperature as shown in Fig. 4*C*. Remarkably, under the low-temperature and high-humidity condition, the temperature increase of H30 can still achieve ∼50 °C and ∼30 °C when solar irradiance is 0.7 $kW{\cdot}m^{-2}$ and 0.3 $kW{\cdot}m^{-2}$, respectively, indicating its excellent environmental suitability, as sufficient sunlight is not always available, especially in humid environments.

Another significant advantage of CR-SASs is the long-term durability (i.e., the photothermal capacity of H30 remained relatively constant even after 100 d), as shown in Fig. 4*D*. For practical applications, it is highly desirable to introduce CR-SAS to different materials including metals and plastics. Hence, we prepared iron oxide nanoparticle-based CR-SASs on Al, Ti, Fe, quartz, alumina, and polypropylene substrates by using PLD with an applied Ar pressure of 30 Pa (*SI Appendix*, Fig. S13). The surface temperatures on the various H30-coated substrates were all higher than 0 °C under the low-temperature and high-humidity condition with one-sun illumination (Fig. 4*E* and *SI Appendix*, Fig. S14), confirming excellent anti-icing/frosting performances on a wide range of materials.

Conclusions

Developing anti-icing materials with high efficiency in inhibiting condensation freezing under high-humidity, low-temperature conditions is highly desirable. Inspired by the strategy of enhancing photosynthetic efficiency on wheat leaves, we have fabricated micro/nano hierarchical structured CR-SASs with enhanced condensate self-removing and efficient solar anti-icing synergistic binary effects. CR-SASs displayed self-propelled droplet jumping driven by the released surface energy via mutual coalescence. The highest R_{wr} of CR-SASs was 1.6 g/m^2 min, leading to a high f_{dry} of ∼80%. Moreover, the micro/nano hierarchical structure of iron oxide nanoparticles endowed CR-SASs with superior anti-reflection and photothermal conversion capabilities. The continuous shedding of condensed water droplets ensured sustained refreshing of dry area available for sunlight absorption and solar-to-heat conversion, maintaining the CR-SAS equilibrium temperature above 0 °C at all times, even under an ambient temperature of −50 °C and ultra-high humidity with an SSD of ∼260. The durability, versatility, and adaptability on different materials carry the potential to open more opportunities for CR-SASs in practical anti-icing applications.

Materials and Methods

Surface Fabrication. To fabricate CR-SASs, a PLD system consisting of a 70 W picosecond laser (12 ps, 1064 nm, Edgewave PX-series), a vacuum chamber, an Ar supply unit, a target, and a substrate (Fig. 1*A*) was employed. In the vacuum chamber, the Ar pressure (99.9% purity, purchased from Laike Kaite Company) was maintained at 10 to 30 Pa. Then, a focused ultrafast laser

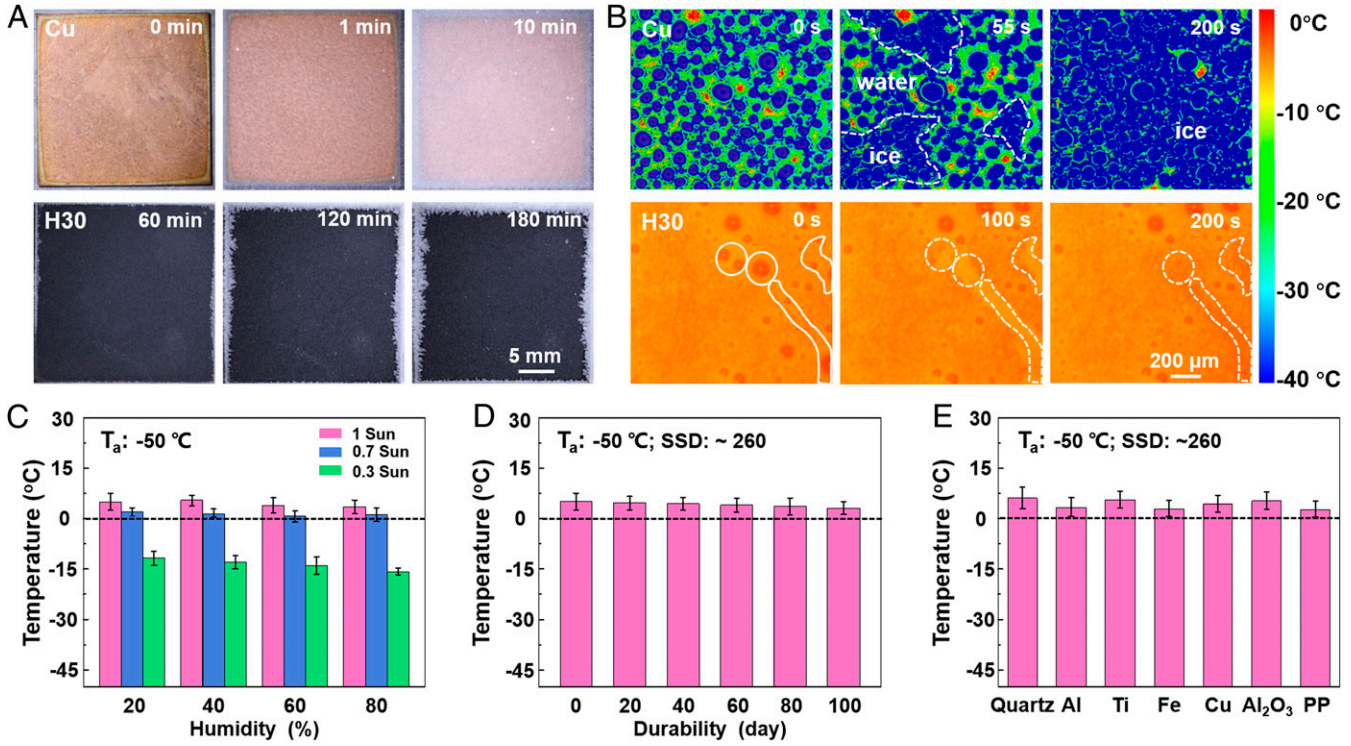

Fig. 4. Durability and versatility of CR-SASs. (*A*) Long-period photothermal experiment under the low-temperature and high-humidity condition for Cu and H30. (*B*) Time lapse Infrared (IR) images showing the dynamic water condensation, removal, and freezing process of Cu and H30 under the low-temperature and high-humidity condition. (*C*) The equilibrium surface temperature of H30 at different humidity and solar irradiance. (*D*) The stability of the photothermal capacity of H30 after 100 d, showing minimal degradation. (*E*) Greater than 50 °C surface temperature increases achieved on CR-SASs with different substrate materials under the low-temperature and high-humidity condition.

beam ablated the target at 70 W and 300 kHz with an ablation path controlled by a galvanometer (SCANLAB intelliSCAN). The Gaussian laser spot diameter was 112 μm, and the scanning speed was 1 m/s. The target material was iron with a purity of 99.5% (purchased from Zhongnuo Xincai Company), and the substrates were polished copper plates with a size of 25 mm × 25 mm and a thickness of 1 mm. The distance between the substrate and the target was 80 mm. By adjusting the Ar pressure within the vacuum chamber, hierarchically structured CR-SASs with different morphologies were fabricated.

For microstructured surfaces, Cu plates (99.5% in purity, 25 mm × 25 mm) were irradiated with a 70 W picosecond laser. To obtain surfaces with microcone arrays, a grid path was scanned by a two-mirror galvanometer (Scanlab Intellicube 14) with an F-Theta objective lens ($f = 55$ mm) in a clean room under an atmospheric environment. The grid path consisted of multiple scans in horizontal (x) and vertical (y) directions. The average output laser power was 1.2 W, and the scanning speed of the galvanometer was fixed at 1 m/s. The spacing between adjacent laser scanning paths was 20 μm, and the number of scans for M1 and M2 were 20 and 40, respectively, resulting in different microcone heights.

Surface Characterization. The morphology of CR-SASs was carefully examined using a field-emission scanning electron microscope (SEM, Zeiss Merlin) with energy dispersive spectroscopy (EDS, Oxford). The contact angle measurements were performed using a video-based optical contact angle measuring device (OCA 15 Plus from DataPhysics Instruments) and the sessile drop (3.5 μL) method. An average of three independently measured contact angles for each CR-SAS was recorded. The surface composition of CR-SASs was characterized with XPS combined with ion sputtering (ESCALAB250XI, VG Instruments).

Coalesced Droplet-Jumping Experiment. The coalesced droplet-jumping process was recorded by a microdroplet dispensing and visualizing system developed by Yan et al. (23) The system consists of a piezoelectric pulse injector integrated in a micro goniometer (MCA-3, Kyowa Interface Science). To prepare two microdroplets positioned side by side, the piezoelectric injector was placed above a CR-SAS (in this case H30) and turned on to dispense microscale droplets. After droplet coalescence, the jumping process was recorded by a high-speed camera (Phantom v711, Vision Research). All experiments were conducted at an ambient environment temperature (24.0 ± 1.0 °C) and relative humidity (40 ± 5%).

Condensation Experiment. The samples were bonded with thermal paste onto a cryostage, in which the ambient temperature and relative humidity were 24.0 ± 1.0 °C and 40 ± 5%, respectively. The temperature of the cryostage was controlled by a cooling unit (low-temperature stirring reaction bath, DHJF Series) and was set to 1.0 ± 0.5 °C, as shown in *SI Appendix*, Fig. S5. Three condensation tests were conducted on each of the prepared samples. The observing optical system consists of a 10× magnifying optical lens (Olympus), a high-speed video camera (Phantom v7.3), and a custom-made coaxial light source to obtain high contrast image between the droplet (bright) and the substrate (dark). The condensation process for each experiment was recorded at 10 fps for 10 min, in which time 0 refers to when the cryostage was cooled to 1 °C at a cooling rate of 10 °C/min. The R_{wr} for each surface was calculated using an algorithm developed by Zhao et al. (47), and the f_{dry} over time was obtained through manually counting and calculating the percentage of water coverage area with respect to the total surface area using Nanomeasure.

Photothermal Experiment under Dry Condition. Samples were placed onto a rotatable platform. A sun simulator (LED light source, TSPA22 × 8, AITEC-SYSTEM) was employed to provide different light intensity, and the temperatures of the samples were monitored and recorded with an infrared camera (Fluke TiS55), as shown in *SI Appendix*, Fig. S8. The ambient temperature and relative humidity were 23.0 ± 1.0 °C and 45 ± 5%, respectively.

Modeling and Simulation. The heat transfer simulations were carried out with ANSYS FLUENT 6.3 software. In the modeling, the temperature distribution of CR-SASs with different fraction of dry area (f_{dry}) under one-sun illumination was simulated. The simulation condition closely imitated the experimental system, in which samples were placed onto a thermal insulation plank (3 mm

thick) in a closed quartz chamber with temperature kept at 223 K on the upper and side walls. The light source was placed above the chamber to illuminate the samples. The incident angle was 0° (q = 1.0 kW/m^2). The length, width, and thickness of the samples were 25 mm, 25 mm, and 1 mm, respectively. The initial temperature of the model was set as 223 K. The light that transmits the atomized droplets cannot be simulated. Thus, we only considered the photothermal effect of the dry area. The calculation was done by directly converting the percentage of heat absorbed by the dry area into the absorption rate of the whole surface. The whole simulation chamber was closed. The temperature of the upper and surrounding boundary was set as 223 K. The other parts of the system were set as thermally insulating.

The governing equation of airflow and temperature fields are shown as follows:

$$\rho_0 \frac{dV}{dt} = \rho g - \nabla p + \mu \nabla^2 V \quad [1]$$

$$\rho_0 C_p \frac{dT}{dt} = \lambda \nabla^2 T + S, \quad [2]$$

where μ is the air dynamic viscosity, λ is the thermal conductivity, and S is the source item. Here, Boussinesq approximation was applied to calculate the natural convection of air, in which the density of gravity term is given by:

$$\rho = \rho_0[1 - \alpha(T - T_0)], \quad [3]$$

where α is expansion coefficient, set as 0.0027 1/k, and ρ_0 and T_0 are reference density and temperature (−30 °C), respectively. The solid film is thermal conductive inside, and the bottom of substrate is heat insulating, in which heat transfer can be expressed in the following equation.

$$\rho_0 C_p \frac{\partial V}{\partial t} = \lambda \nabla^2 T + q. \quad [4]$$

The temperature, velocity magnitude, and static pressure contours in the cross-section direction when the experimental system reaches equilibrium were obtained, as shown in *SI Appendix*, Fig. S11.

Photothermal Experiment under the Low-Temperature and High-Humidity Condition. The sample was placed inside a quartz chamber. Liquid ethanol was introduced to the wall cavity of the quartz chamber by a cooling unit (DHJF Series), in which the temperature inside the chamber could be controlled (50). The sample was then kept within the chamber until its temperature reached the temperature inside the chamber. Upon solar irradiation, the temperature increase of the sample was measured and recorded by a thermocouple, which was bonded to the sample using thermal paste. At the onset of solar heating, wet air was introduced into the chamber, as illustrated in *SI Appendix*, Fig. S12, and the humidity was adjusted by controlling the air flux. Herein, the low-temperature and high-humidity condition is defined to be when the temperature inside the quartz chamber is −50.0 ± 1.0 °C and the relative humidity of the input wet air is 80 ± 5%. It should be noted that the relative humidity for the input wet air was measured at room temperature (24.0 ± 1.0 °C), which corresponds to an extremely high supersaturation degree of around 260 at the sample surface. Hence, the inside of the chamber was highly supersaturated, mimicking the condition in which the formation of rime occurs. In addition, the dynamic water condensing, removing, and freezing processes on H30 and Cu surfaces were observed using a high-resolution infrared camera (X8503sc, FLIR), and the sample rate was 5 Hz.

Data Availability. All study data are included in the article and/or supporting information.

ACKNOWLEDGMENTS. We gratefully acknowledge the financial support from the National Key Research and Development Program of China (2020YFE0100300, 2018YFA0208502, and 2017YFB1104900), Chinese National Nature Science Foundation (21875261, 51925307, 21733010, 21805286, and 52005022), Key Research Program of Frontier Sciences, CAS, Grant No. ZDBS-LYSLH031, the Youth Innovation Promotion Association of the Chinese Academy of Sciences (2018044), NSF CAREER award (1724526), and AFOSR awards (FA9550-17-1-0311, FA9550-18-1-0449, and FA9550-20-1-0344). We are grateful to the Energy Transport Research Laboratory at the University of Illinois Urbana–Champaign for conducting side-view experiments of droplet coalescence and jumping as well as the experiments for dynamic water condensing, removing, and freezing processes.

1. M. J. Kreder, J. Alvarenga, P. Kim, J. Aizenberg, Design of anti-icing surfaces: Smooth, textured or slippery? *Nat. Rev. Mater.* **1**, 15003 (2016).
2. K. Golovin, A. Dhyani, M. D. Thouless, A. Tuteja, Low-interfacial toughness materials for effective large-scale deicing. *Science* **364**, 371–375 (2019).
3. T.-S. Wong *et al*., Bioinspired self-repairing slippery surfaces with pressure-stable omniphobicity. *Nature* **477**, 443–447 (2011).
4. Z. He, K. Liu, J. Wang, Bioinspired materials for controlling ice nucleation, growth, and recrystallization. *Acc. Chem. Res.* **51**, 1082–1091 (2018).
5. T. Wang *et al*., Passive anti-icing and active deicing films. *ACS Appl. Mater. Interfaces* **8**, 14169–14173 (2016).
6. D. M. Ramakrishna, T. Viraraghavan, Environmental impact of chemical deicers – a review. *Water Air Soil Pollut.* **166**, 49–63 (2005).
7. C. Walker *et al*., Desublimation frosting on nanoengineered surfaces. *ACS Nano* **12**, 8288–8296 (2018).
8. S. Anand, A. T. Paxson, R. Dhiman, J. D. Smith, K. K. Varanasi, Enhanced condensation on lubricant-impregnated nanotextured surfaces. *ACS Nano* **6**, 10122–10129 (2012).
9. J. B. Boreyko, C. P. Collier, Delayed frost growth on jumping-drop superhydrophobic surfaces. *ACS Nano* **7**, 1618–1627 (2013).
10. J. Cui, D. Daniel, A. Grinthal, K. Lin, J. Aizenberg, Dynamic polymer systems with self-regulated secretion for the control of surface properties and material healing. *Nat. Mater.* **14**, 790–795 (2015).
11. R. Dou *et al*., Anti-icing coating with an aqueous lubricating layer. *ACS Appl. Mater. Interfaces* **6**, 6998–7003 (2014).
12. J. Chen, Z. Luo, Q. Fan, J. Lv, J. Wang, Anti-ice coating inspired by ice skating. *Small* **10**, 4693–4699 (2014).
13. J. Chen *et al*., Robust prototypical anti-icing coatings with a self-lubricating liquid water layer between ice and substrate. *ACS Appl. Mater. Interfaces* **5**, 4026–4030 (2013).
14. J. Lv, Y. Song, L. Jiang, J. Wang, Bio-inspired strategies for anti-icing. *ACS Nano* **8**, 3152–3169 (2014).
15. S. Jung *et al*., Are superhydrophobic surfaces best for icephobicity? *Langmuir* **27**, 3059–3066 (2011).
16. K. K. Varanasi, T. Deng, J. D. Smith, M. Hsu, N. Bhate, Frost formation and ice adhesion on superhydrophobic surfaces. *Appl. Phys. Lett.* **97**, 234102 (2010).
17. Y.-T. Cheng, D. E. Rodak, Is the lotus leaf superhydrophobic? *Appl. Phys. Lett.* **86**, 144101 (2005).
18. A. Pringle, S. N. Patek, M. Fischer, J. Stolze, N. P. Money, The captured launch of a ballistospore. *Mycologia* **97**, 866–871 (2005).
19. J. B. Boreyko, C.-H. Chen, Self-propelled dropwise condensate on superhydrophobic surfaces. *Phys. Rev. Lett.* **103**, 184501 (2009).
20. K. Rykaczewski *et al*., How nanorough is rough enough to make a surface superhydrophobic during water condensation? *Soft Matter* **8**, 8786–8794 (2012).
21. Q. Zhang *et al*., Anti-icing surfaces based on enhanced self-propelled jumping of condensed water microdroplets. *Chem. Commun. (Camb.)* **49**, 4516–4518 (2013).
22. N. Miljkovic *et al*., Jumping-droplet-enhanced condensation on scalable superhydrophobic nanostructured surfaces. *Nano Lett.* **13**, 179–187 (2013).
23. X. Yan *et al*., Droplet jumping: Effects of droplet size, surface structure, pinning, and liquid properties. *ACS Nano* **13**, 1309–1323 (2019).
24. J. Liu *et al*., Guided self-propelled leaping of droplets on a micro-anisotropic superhydrophobic surface. *Angew. Chem. Int. Ed. Engl.* **55**, 4265–4269 (2016).
25. K. Wang *et al*., Self-enhancement of droplet jumping velocity: The interaction of liquid bridge and surface texture. *RSC Adv.* **6**, 99314–99321 (2016).
26. Q. Xu, J. Li, J. Tian, J. Zhu, X. Gao, Energy-effective frost-free coatings based on superhydrophobic aligned nanocones. *ACS Appl. Mater. Interfaces* **6**, 8976–8980 (2014).
27. Z. Wang, Recent progress on ultrasonic de-icing technique used for wind power generation, high-voltage transmission line and aircraft. *Energy Build.* **140**, 42–49 (2017).
28. E. Mitridis *et al*., Metasurfaces leveraging solar energy for icephobicity. *ACS Nano* **12**, 7009–7017 (2018).
29. C. Walker *et al*., Transparent metasurfaces counteracting fogging by harnessing sunlight. *Nano Lett.* **19**, 1595–1604 (2019).
30. S. Dash, J. de Ruiter, K. K. Varanasi, Photothermal trap utilizing solar illumination for ice mitigation. *Sci. Adv.* **4**, eaat0127 (2018).
31. G. Jiang, L. Chen, S. Zhang, H. Huang, Superhydrophobic SiC/CNTs coatings with photothermal deicing and passive anti-icing properties. *ACS Appl. Mater. Interfaces* **10**, 36505–36511 (2018).
32. L. Ma *et al*., Plasmon-mediated photothermal and superhydrophobic TiN-PTFE film for anti-icing/deicing applications. *Compos. Sci. Technol.* **181**, 107696 (2019).
33. G. Zhang, Q. Zhang, T. Cheng, X. Zhan, F. Chen, Polyols-infused slippery surfaces based on magnetic Fe_3O_4-functionalized polymer hybrids for enhanced multifunctional anti-icing and deicing properties. *Langmuir* **34**, 4052–4058 (2018).
34. T. Cheng, R. He, Q. Zhang, X. Zhan, F. Chen, Magnetic particle-based superhydrophobic coatings with excellent anti-icing and thermoresponsive deicing performance. *J. Mater. Chem. A Mater. Energy Sustain.* **3**, 21637–21646 (2015).
35. C. Feng *et al*., A bioinspired, highly transparent surface with dry-style antifogging, antifrosting, antifouling, and moisture self-cleaning properties. *Macromol. Rapid Commun.* **40**, e1800708 (2019).
36. S. Wu *et al*., Superhydrophobic photothermal icephobic surfaces based on candle soot. *Proc. Natl. Acad. Sci. U.S.A.* **117**, 11240–11246 (2020).
37. L. Yao, J. He, Recent progress in antireflection and self-cleaning technology-From surface engineering to functional surfaces. *Prog. Mater. Sci.* **61**, 94–143 (2014).
38. K. Manabe *et al*., Antifibrinogen, antireflective, antifogging surfaces with biocompatible nano-ordered hierarchical texture fabricated by layer-by-layer self-assembly. *Chem. Mater.* **29**, 4745–4753 (2017).

39. S. Nath *et al*., 'Sneezing' plants: Pathogen transport via jumping-droplet condensation. *J. R. Soc. Interface* **16**, 20190243 (2019).
40. G. Zhao *et al*., Competing effects between condensation and self-removal of water droplets determine antifrosting performance of superhydrophobic surfaces. *ACS Appl. Mater. Interfaces* **12**, 7805–7814 (2020).
41. D. Riabinina, E. Irissou, B. Le Drogoff, M. Chaker, D. Guay, Influence of pressure on the Pt nanoparticle growth modes during pulsed laser ablation. *J. Appl. Phys.* **108**, 034322 (2010).
42. B. Feng *et al*., Cooperative bilayer of lattice-disordered nanoparticles as room-temperature sinterable nanoarchitecture for device integrations. *ACS Appl. Mater. Interfaces* **11**, 16972–16980 (2019).
43. W. Zhao *et al*., Super black iron nanostructures with broadband ultralow reflectance for efficient photothermal conversion. *Appl. Surf. Sci.* **521**, 146388 (2020).
44. M. D. Mulroe, B. R. Srijanto, S. F. Ahmadi, C. P. Collier, J. B. Boreyko, Tuning superhydrophobic nanostructures to enhance jumping-droplet condensation. *ACS Nano* **11**, 8499–8510 (2017).
45. R. Wang *et al*., Bio-inspired superhydrophobic closely packed aligned nanoneedle architectures for enhancing condensation heat transfer. *Adv. Funct. Mater.* **28**, 1800634 (2018).
46. T. M. Schutzius *et al*., Spontaneous droplet trampolining on rigid superhydrophobic surfaces. *Nature* **527**, 82–85 (2015).
47. G. Zhao *et al*., Rationally designed surface microstructural features for enhanced droplet jumping and anti-frosting performance. *Soft Matter* **16**, 4462–4476 (2020).
48. J. Long *et al*., Cassie-state stability of metallic superhydrophobic surfaces with various micro/nanostructures produced by a femtosecond laser. *Langmuir* **32**, 1065–1072 (2016).
49. K. M. Wisdom *et al*., Self-cleaning of superhydrophobic surfaces by self-propelled jumping condensate. *Proc. Natl. Acad. Sci. U.S.A.* **110**, 7992–7997 (2013).
50. J. Liu *et al*., Distinct ice patterns on solid surfaces with various wettabilities. *Proc. Natl. Acad. Sci. U.S.A.* **114**, 11285–11290 (2017).